

# Low-Power Bistability in Graphene-Comprising 3D Photonic Resonant Circuits

Thomas Christopoulos,<sup>1, a)</sup> Odysseas Tsilipakos,<sup>2</sup> and Emmanouil E. Kriezis<sup>1</sup>

<sup>1)</sup>*Department of Electrical and Computer Engineering, Aristotle University of Thessaloniki (AUTH), Thessaloniki 54124, Greece*

<sup>2)</sup>*Institute of Electronic Structure and Laser, Foundation for Research and Technology Hellas (FORTH), Heraklion 71110, Crete, Greece*

(Dated: 21 November 2017)

Practical graphene-comprising resonant structures are proposed for high-quality Kerr-induced bistability with low input power. Two structures are designed for operation in the far-infrared (FIR) and near-infrared (NIR) frequency regimes, respectively. The nonlinear response is studied by utilizing a theoretical framework combining perturbation theory and coupled-mode theory, capable of accurately and efficiently modeling resonant structures with dispersive bulk and sheet materials. The FIR system is based on a side-coupled graphene-nanoribbon ring resonator, formed by applying a bias voltage between a uniform graphene sheet and an uneven silicon substrate. By optimizing the system geometry, we demonstrate bistable response with theoretically infinite extinction ratio between states and an operating power of only 400  $\mu$ W at 10 THz. In the NIR circuit, a silicon photonic ring resonator is overlaid with a graphene sheet. The silicon-slot geometry is judiciously chosen to maximize the field overlap with graphene, resulting in low power requirements of 90 mW at 1.55  $\mu$ m. In both cases, nonlinearity stems from the instantaneous Kerr effect in graphene, allowing for ultra-fast response. Combining low input power and fast response times, the proposed components highlight the potential of graphene for nonlinear applications over a broad spectral range.

PACS numbers: 42.65.Pc, 42.65.Hw, 42.82.-m, 73.20.Mf

## I. INTRODUCTION

Nonlinear phenomena have attracted great interest in recent years, especially in the context of guided-wave silicon photonic<sup>1</sup> and plasmonic<sup>2</sup> technologies which allow for strong light confinement favoring their manifestation. Among the plethora of available nonlinearities, of utmost importance are the instantaneous  $\chi^{(3)}$  phenomena, which can lead to ultra-fast all-optical operation. Especially when combined with optical feedback (provided by a resonant structure), they allow for bistable response, paving the way for memory,<sup>3</sup> switching,<sup>4,5</sup> and logic gate<sup>6,7</sup> applications. Interestingly, ideas from linear resonant structures, such as Fano resonances and electromagnetically-induced transparency, can be also employed to enhance the device performance.<sup>8,9</sup>

Early works on optical bistability in guided-wave photonics focused on photonic crystal resonators implemented with the silicon-on-insulator technology.<sup>3-5,8,10</sup> In plasmonics, studies mainly revolved around the metal-insulator-metal platform.<sup>11,12</sup> In both cases, 2D geometries were typically analyzed for demonstrating the potential of each technology for nonlinear applications. Lately, more practical, 3D structures based on a hybrid silicon-plasmonic technology were proposed. Side-coupled standing-<sup>13</sup> and traveling-wave<sup>14</sup> resonators were examined, while complex phenomena involving free carriers in silicon were also investigated.<sup>15</sup>

Providing low power requirements and at the same time ultra-fast response requires highly nonlinear materials. In Refs. 13–15 this requirement was addressed by utilizing a highly nonlinear polymer. A different approach would be to exploit the exotic nonlinear properties of graphene which has recently permeated the field of photonics.<sup>16</sup> Graphene exhibits exceptionally strong Kerr-type nonlinearity over a vast frequency range, spanning from the near-infrared (NIR) to the far-infrared (FIR) frequency regime.<sup>17-20</sup> As a result, this has triggered an interest in graphene-comprising resonators for nonlinear applications.<sup>21-24</sup>

In this work, we demonstrate three-dimensional, practical graphene-comprising resonant structures with bistable response. Two examples are provided for operation in the NIR and FIR regime, respectively, accounting for two-photon absorption and the effect of free carriers emanating from the silicon bulk regions. In both cases, the structures are carefully designed to exhibit low power requirements and ultra-fast response. We make use of a recently-developed mathematical framework combining perturbation theory and coupled-mode theory (CMT), allowing for rigorous modeling of nonlinear resonators comprising both bulk (3D) and sheet (2D) materials,<sup>25</sup> carefully expanded to include nonlinear loss. This framework is efficient and highly accurate, as demonstrated by comparing with nonlinear finite-element (FEM) simulations.<sup>25</sup>

The paper is organized as follows: The theoretical framework is briefly presented in Sec. II, expanded to include two-photon absorption (TPA). In Sec. III a nonlinear 3D graphene-nanoribbon-based (GNR) ring resonator

---

<sup>a)</sup>Electronic mail: cthomasa@ece.auth.gr

is proposed. At THz frequencies graphene supports strongly-confined surface plasmon polaritons (SPPs) allowing for significant field enhancement which, combined with the strong nonlinearity it exhibits, leads to sub-mW bistability at 10 THz. In the NIR circuit presented in Sec. IV a silicon-slot platform is used to guide the light-wave. Graphene is incorporated for contributing its high nonlinearity; Kerr-induced optical bistability is obtained for an input power of only 90 mW at 1.55  $\mu\text{m}$ . Finally, the results are summarized and discussed in Sec. V.

## II. THEORETICAL FRAMEWORK

For analyzing the proposed graphene-comprising resonant systems we employ a theoretical framework combining perturbation theory and coupled-mode theory, recently introduced in Ref. 25. The former is used to estimate the small, nonlinearly-induced, change in the resonator properties (resonant frequency, quality factor) by conducting linear full-wave simulations.<sup>25,26</sup> The latter is subsequently utilized to calculate the nonlinear response of the resonant system.<sup>10,14,27</sup>

### A. Perturbation Theory

Perturbation theory dictates how a small, linearly- or nonlinearly-induced, modification in the properties of a system alters the macroscopic parameters that characterize it.<sup>26,28</sup> In the context of resonant structures, we are interested in the nonlinear frequency shift  $\Delta\omega$ . Treating the most general case involving anisotropic materials with complex and dispersive electrical permittivity and conductivity, perturbation theory indicates that the (complex in general) nonlinear frequency shift, induced by polarization and current density nonlinearities, is given by<sup>25</sup>

$$\frac{\Delta\omega}{\omega_0} = - \frac{\int_V \mathbf{P}_{\text{NL}} \cdot \mathbf{E}_0^* dV - j \frac{1}{\omega_0} \int_V \mathbf{J}_{\text{NL}} \cdot \mathbf{E}_0^* dV}{\int_V \frac{\partial \left\{ \omega \varepsilon_0 \bar{\varepsilon}_r + \bar{\sigma}_{\text{Im}}^{(1)} \right\}}{\partial \omega} \mathbf{E}_0 \cdot \mathbf{E}_0^* dV + \mu_0 \int_V \mathbf{H}_0 \cdot \mathbf{H}_0^* dV}, \quad (1)$$

for  $\exp\{+j\omega t\}$  harmonic time convention. In Eq. (1)  $\mathbf{P}_{\text{NL}}$  stands for the nonlinear polarization, corresponding to dielectric nonlinearities (nonlinear motion of bound electrons<sup>29</sup>), and  $\mathbf{J}_{\text{NL}}$  for the nonlinear current density, corresponding to the nonlinear response of free electrons.<sup>20</sup> Importantly, the inclusion of  $\mathbf{J}_{\text{NL}}$  allows for treating nonlinear 2D conductive sheet materials such as graphene. The denominator is proportional to the stored energy in the cavity. Apart from the dispersive electric and magnetic terms, it also comprises an extra term representing the energy stored in the current

density due to the dispersive imaginary part of the electric conductivity.<sup>25</sup> This term is important when highly dispersive conductive materials are considered, such as graphene in the THz.

In this work, we focus on third-order instantaneous nonlinearities, namely the Kerr effect and TPA. Both nonlinear processes can be introduced using the polarization and/or current density terms. Following the procedure outlined in Appendix A, we find the complex nonlinear frequency shift<sup>15,25</sup>

$$\Delta\omega = [-\gamma^{\text{Kerr}} + j\gamma^{\text{TPA}}] W_{\text{res}} = [-(\gamma_b^{\text{Kerr}} + \gamma_s^{\text{Kerr}}) + j(\gamma_b^{\text{TPA}} + \gamma_s^{\text{TPA}})] W_{\text{res}}, \quad (2)$$

where  $W_{\text{res}}$  is the total stored energy in the resonator. The complex nonlinear parameter  $\gamma = -\gamma^{\text{Kerr}} + j\gamma^{\text{TPA}}$  is measured in  $\text{W}^{-1}\text{s}^{-2}$  with real and imaginary parts describing the Kerr and TPA effects, respectively. It is the resonator (3D) counterpart of the widely-known waveguide (2D) nonlinear parameter.<sup>28</sup> In Eq. (2) we distinguish between the contributions of bulk and sheet materials. Note that for  $\gamma^{\text{Kerr}}$  the two contributions can be of different sign depending on the nature of the underlying materials (self- or de-focusing). On the other hand,  $\gamma_s^{\text{TPA}}$  and  $\gamma_b^{\text{TPA}}$  are always positive since they describe a loss mechanism. Also note that each individual  $\gamma$  parameter is proportional to the respective dimensionless nonlinear feedback parameter  $\kappa$  (introduced rigorously in Appendix A), measuring the overlap between the mode and the nonlinear material.

### B. Coupled-Mode Theory

CMT treats a weakly-coupled resonator with relatively low loss (radiation and ohmic) as a lumped oscillator, leading to a readily-solvable first order differential equation.<sup>27</sup> In addition, it allows for including nonlinear effects.<sup>10,14</sup> Specifically, incorporating the complex  $\Delta\omega$  of Eq. (2) (the real part,  $\text{Re}\{\Delta\omega\}$ , corresponds to the Kerr-induced nonlinear frequency shift and the imaginary part,  $\text{Im}\{\Delta\omega\} = 1/\tau_{\text{TPA}}$ , to TPA-induced nonlinear loss) and assuming a side-coupled traveling-wave resonator (practically realized as a ring resonator) we arrive at

$$\frac{da}{dt} = j(\omega_0 - \gamma^{\text{Kerr}}|a|^2) a - \left( \frac{1}{\tau_i} + \frac{1}{\tau_e} + \gamma^{\text{TPA}}|a|^2 \right) a + j\sqrt{\frac{2}{\tau_e}} s_i, \quad (3a)$$

$$s_t = s_i + j\sqrt{\frac{2}{\tau_e}} a, \quad (3b)$$

where  $\tau_i$ ,  $\tau_e$  are cavity photon lifetimes corresponding to intrinsic (resistive and radiation) and external (coupling) loss. The respective quality factors are  $Q = \omega_0\tau/2$ . Cavity amplitude  $a$  is normalized so that  $|a|^2 \equiv W_{\text{res}}$  is the stored energy in the cavity while incident and

transmitted wave amplitudes  $s_i$  and  $s_t$  are normalized so that  $|s|^2$  expresses guided power. It is emphasized that Eq. (3a) can describe a broad range of different photonic resonators (of traveling- or standing-wave type) and account for different feeding schemes by incorporating the pertinent last term; Eq. (3b) is accordingly revised but in all cases accounts for a linear relation between wave and cavity amplitudes.

Equations (3) are easily solvable under appropriate normalization. Letting  $a(t) = \tilde{a}(t)\exp\{+j\omega t\}$ , with  $\tilde{a}$  denoting the slowly-varying envelope (the same approximation is applied to wave amplitudes  $s$ ), and using the normalized quantities  $\tilde{u} = \sqrt{\tau_i}|\gamma^{\text{Kerr}}|\tilde{a}$ ,  $\tilde{\psi} = \sqrt{\tau_i^2|\gamma^{\text{Kerr}}|/2}\tilde{s}$  and  $t' = t/\tau_i$ , we find

$$\frac{d\tilde{u}}{dt'} = -j(\delta + \text{sgn}(\gamma^{\text{Kerr}})|\tilde{u}|^2)\tilde{u} - (1 + r_Q + r_{\text{TPA}}|\tilde{u}|^2)\tilde{u} + j2\sqrt{r_Q}\tilde{\psi}_i, \quad (4a)$$

$$\tilde{\psi}_t = \tilde{\psi}_i + j\sqrt{r_Q}\tilde{u}, \quad (4b)$$

where  $\text{sgn}(\cdot)$  is the sign function,  $\delta = (\omega - \omega_0)\tau_i$  is the normalized detuning parameter,  $r_Q = Q_i/Q_e$  is the quality factor ratio and  $r_{\text{TPA}} = \gamma^{\text{TPA}}/|\gamma^{\text{Kerr}}|$  represents the relative strength of TPA compared to the Kerr effect.

Under continuous wave (CW) conditions, Eqs. (4) can be transformed in a  $2 \times 2$  system of polynomial equations, reading<sup>15</sup>

$$\frac{p_{\text{out}}}{p_{\text{in}}} = \frac{[\delta + \text{sgn}(\gamma^{\text{Kerr}})p_i]^2 + (1 - r_Q + r_{\text{TPA}}p_i)^2}{[\delta + \text{sgn}(\gamma^{\text{Kerr}})p_i]^2 + (1 + r_Q + r_{\text{TPA}}p_i)^2}, \quad (5a)$$

$$p_{\text{TPA}} = r_{\text{TPA}}p_i^2, \quad (5b)$$

with  $p_i = p_{\text{in}} - p_{\text{out}} - p_{\text{TPA}} = |\tilde{u}|^2$  representing intrinsic loss and  $p_{\text{TPA}} = r_{\text{TPA}}|\tilde{u}|^4$  being the (energy dependent) power loss due to TPA. Eqs. (5) are normalized with respect to the system characteristic power

$$P_0 = \frac{2}{\tau_i^2|\gamma^{\text{Kerr}}|}, \quad (6)$$

which constitutes a measure of the input power that is needed for the nonlinearity to manifest.

For appropriate frequency and input power, the system of Eqs. (5) exhibits three (two stable and one unstable) real, positive solutions, denoting bistable response. Following Ref. 15, we find that the necessary condition is  $\delta < -\delta_{\text{th}}$  or  $\delta > \delta_{\text{th}}$  depending on the sign of  $\gamma^{\text{Kerr}}$ . The first inequality corresponds to self-focusing materials ( $\gamma^{\text{Kerr}} > 0$ ; red-shifting of the resonant frequency) while the second to de-focusing materials ( $\gamma^{\text{Kerr}} < 0$ ; blue-shifting of the resonant frequency). The detuning threshold is given by

$$\delta_{\text{th}} = \frac{(1 + r_Q)(\sqrt{3} + r_{\text{TPA}})}{1 - \sqrt{3}r_{\text{TPA}}}. \quad (7)$$

When designing bistable systems, an important performance characteristic is the extinction ratio (ER) between

bistable states. In side-coupled traveling-wave resonators zero transmission is obtained under critical coupling. For low input power (linear regime) this condition implies that intrinsic and external losses are equal, i.e.  $r_Q = 1$ . For higher input power, on the other hand, TPA-induced loss is present, modifying the critical coupling condition. It can be recovered by taking TPA into account and satisfying the condition  $1/\tau_i + \gamma_{\text{TPA}}|a|^2 = 1/\tau_e$ , or

$$r_Q = 1 + r_{\text{TPA}}|\tilde{u}|^2. \quad (8)$$

Equation (8) depends on the (normalized) stored energy and it is met exactly only for a specific input power. To determine it we calculate the transmission versus input power using CMT for a chosen detuning  $\delta$  and  $r_Q = 1$ . In that curve, we seek for the minimum transmission point and the respective stored energy. Using the latter, we revise the value of  $r_Q$  and repeat the process. After a few iterations, the modified critical coupling condition is determined. Note that for low input power ( $|\tilde{u}|^2 \rightarrow 0$ ) or weak TPA ( $r_{\text{TPA}} \rightarrow 0$ ),  $r_Q = 1$  is recovered.

### III. FAR-INFRARED (THz) REGIME

Having established the framework, we first focus on the FIR (THz) regime. In this case, graphene is used for both forming the guided-wave circuit as well as providing the nonlinearity.

#### A. Graphene Nanoribbon Waveguide

Graphene in the FIR supports SPPs and can thus provide the waveguiding mechanism. Its linear conductivity has a highly-dispersive, Drude-like response due to the intraband absorption process, with an imaginary part that is strongly negative leading to the formation of tightly-confined SPPs. The contribution of the interband term is negligible, even when the Fermi level ( $\mu_c$ ) only slightly deviates from zero. This is due to the very low energy of the THz photons which cannot give rise to interband transitions. Linear loss saturation (i.e., saturable absorption) is also not observed under moderate input power for the same reason.<sup>30</sup> Finally, the third-order nonlinear conductivity of graphene,  $\sigma_3$ , is purely imaginary,<sup>20</sup> meaning that neither interband (due to low photon energy) nor intraband (physically not acceptable) TPA mechanism is present.<sup>31</sup> Note that  $\text{Im}\{\sigma_3\}$  is always positive for  $\mu_c > 0$ , indicating that graphene acts as a self-focusing material in the FIR. The linear and nonlinear properties of graphene are summarized in Appendix B.

The underlying waveguide for forming the resonant circuit is depicted in Fig. 1(a). Starting from a uniform graphene sheet, we spatially confine the supported SPP mode by modifying its conductivity along the  $y$ -axis. To this end, we apply a bias voltage between graphene and a silicon substrate beneath it, at a separating distance

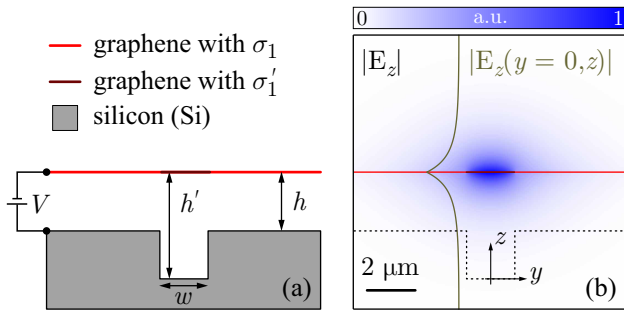


FIG. 1. (a) Graphene nanoribbon formed on an infinite graphene sheet by modifying its conductivity. A bias voltage is applied between the graphene sheet and an uneven silicon substrate. (b) Supported mode profile when  $w = 2 \mu\text{m}$ .

$h$  [Fig. 1(a)]. This capacitor-like structure accumulates charges, setting the graphene Fermi level to 0.7 eV for moderate biasing,<sup>32–34</sup> resulting in a conductivity  $\sigma_1$  at 10 THz. The height  $h$  is directly related to applied voltage  $V$  and to the dielectric constant of the material occupying the space between the graphene layer and the silicon substrate. Exploiting a high- $\kappa$  dielectric can favorably reduce the voltage requirements; a simple capacitor model predicts that a Fermi level of 0.7 eV is possible at a voltage level of 50 V for  $h = 0.6 \mu\text{m}$ , if the dielectric is selected to be  $\text{TiO}_2$  ( $\epsilon_r = 80$ ). By etching the silicon substrate while keeping the DC bias constant, the Fermi level is modified. For  $h' = 5h$  we get  $\mu_c = 0.3 \text{ eV}$  and a conductivity of  $\sigma'_1$  is obtained. The supported SPP is spatially confined in the low Fermi level area where the effective mode index is higher [Fig. 1(b)]. The exact linear and nonlinear conductivity values for the different  $\mu_c$  are presented in Table III of Appendix B.

## B. Ring-Waveguide System Design and Performance

Relying on the GNR waveguide of Fig. 1, a resonant circuit of a ring resonator side-coupled to a bus waveguide is formed, Fig. 2. The geometrical parameters of the resonator are  $w = 2 \mu\text{m}$  and radius  $R$  (measured at the middle of the GNR). The straight bus waveguide is at a coupling distance  $g$  (measured from the resonator outer edge to the waveguide inner edge), while its width is set to  $w_{\text{wg}} = 1.4 \mu\text{m}$  to ensure single mode operation. The uneven ground is omitted in the simulations, since the SPP is tightly confined.

Optimum performance of the resonant system is obtained when its characteristic power is minimized. Combining Eqs. (6) and (A3), a proportionality relation is found:  $P_0 \propto (\kappa_s^{\text{Kerr}} Q_i^2)^{-1}$ . Seeking the radius that provides the minimum  $P_0$  around the frequency of 10 THz, we conduct vectorial FEM eigenvalue simulations of the uncoupled ring, using COMSOL Multiphysics®, to calculate the nonlinear feedback parameter and the intrinsic quality factor. The resonance mode azimuthal order  $m$

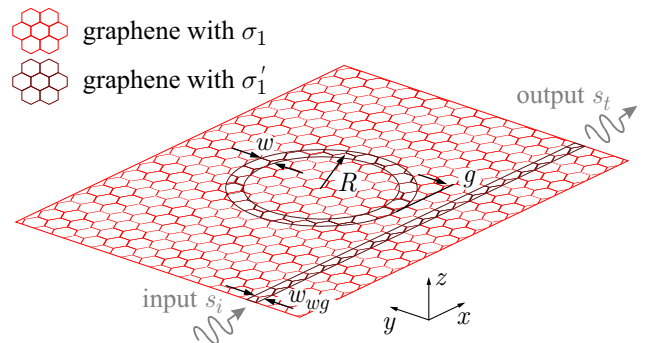


FIG. 2. GNR-based ring resonator, side-coupled to a bus waveguide. The spatial conductivity modulation is achieved by using an uneven substrate, as shown in Fig. 1.

TABLE I. Resonator radius  $R$  and resonance frequencies  $f_0$  for various mode orders  $m$  of the GNR-based ring resonator for the case of taking into account or neglecting graphene dispersion.

$m$	$R$ ( $\mu\text{m}$ )	$f_0^{\text{disp}}$ (THz)	$f_0^{\text{non}}$ (THz)
11	7.3	10.040	10.053
12	8.0	10.033	10.038
13	8.7	10.026	10.025
14	9.4	10.019	10.012
15	10.1	10.014	10.001
16	10.8	10.008	9.990
17	11.5	10.004	9.981
18	12.2	9.999	9.972
19	12.9	9.995	9.965

with the respective radius  $R$  and resonance frequencies  $f_0$  (when graphene dispersion is taken into account or not) are shown in Table I. In the GNR-based ring resonator no other materials interact with the SPP and thus only  $\kappa_s^{\text{Kerr}}$  is nonzero. The nonlinear surface feedback parameter  $\kappa_s^{\text{Kerr}}$  with respect to  $m$  is shown in Fig. 3(a) when dispersion is included (solid line) or not (dashed line). The 4-fold difference between the two reflects the fact that the energy stored on the dispersive graphene sheet is important and thus erroneously set to zero when dispersion is neglected. In both cases,  $\kappa_s^{\text{Kerr}}$  decreases with  $m$  (or equivalently with radius, cf. Table I) because modes with higher azimuthal order are accompanied by higher effective mode volumes, resulting in lower power densities (for a given input power level) and thus weaker electric field amplitudes on graphene.

On the other hand,  $Q_i$  [Fig. 3(b)] increases with  $m$  (since radiation loss is suppressed for higher radii) until reaching an upper limit set by resistive loss. For the calculation of the  $Q$ -factor, we use its definition

$$Q = \omega_0 \frac{W_{\text{res}}}{P}, \quad (9)$$

enclosing the computational domain with a perfectly matched layer (PML) to ensure the correct estimation of radiation loss. In the dispersionless case, the result

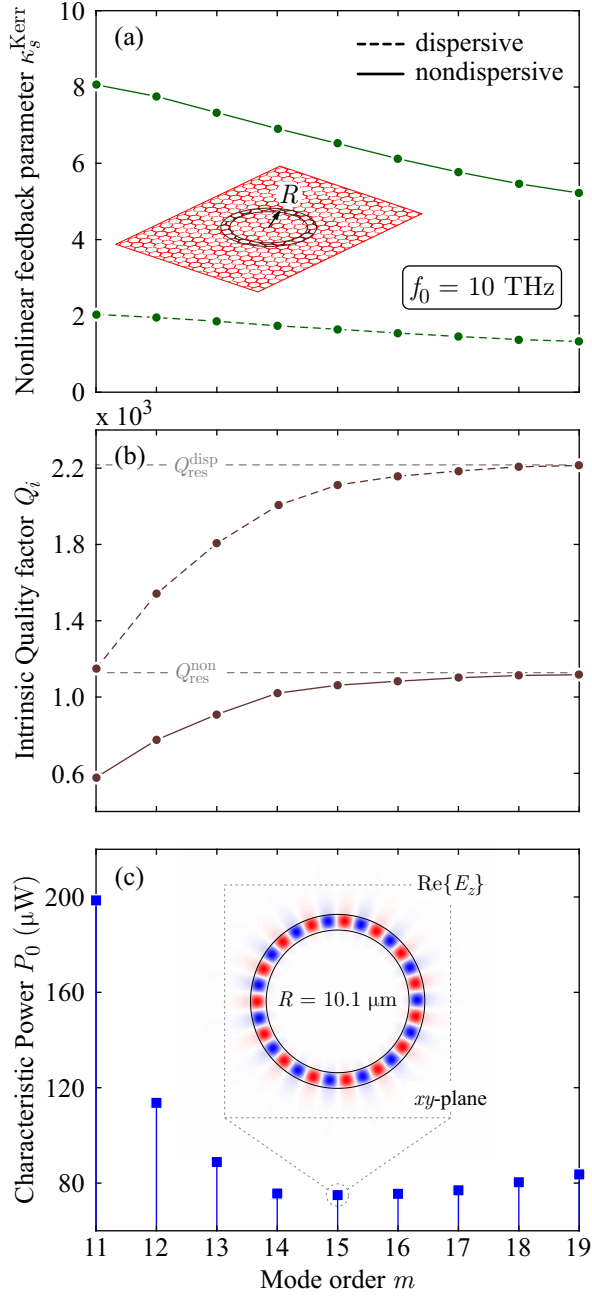


FIG. 3. (a) Nonlinear surface feedback parameter  $\kappa_s^{\text{Kerr}}$  vs mode order  $m$ . (b) Intrinsic quality factor  $Q_i$  vs  $m$ . (c) System characteristic power  $P_0$  vs  $m$ . Opposite trends in  $\kappa_s^{\text{Kerr}}$  and  $Q_i$  result in a minimum  $P_0 = 75.6 \mu\text{W}$  for  $m = 15$  ( $R = 10.1 \mu\text{m}$ ). Inset:  $\text{Re}\{E_z\}$  for the optimum mode. Dashed (solid) lines refer to the dispersive (nondispersive) case ( $P_0$  is the same in both cases). All quantities are discrete; the solid/dashed lines are used to guide the eye.

coincides with the value obtained from the respective eigenfrequency  $\omega$  through  $Q_i = \text{Re}\{\omega\}/2\text{Im}\{\omega\}$ . However, this is not true for the dispersive case, since the solution of an eigenvalue problem cannot take into account material dispersion.<sup>35</sup> Therefore, in such cases the definition should be employed taking care that the proper

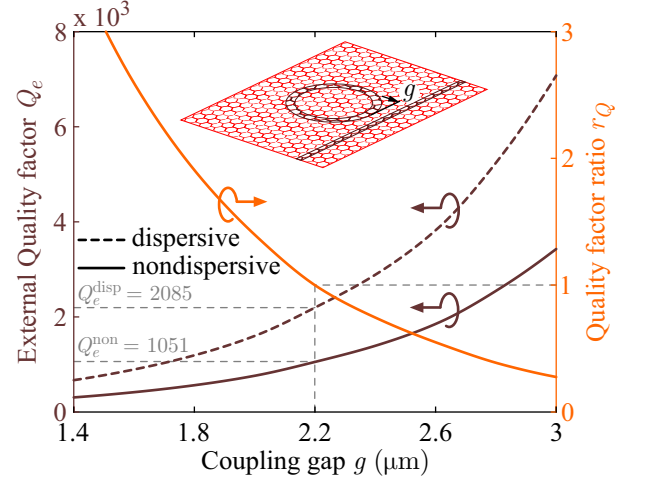


FIG. 4. External quality factor  $Q_e$  and quality factor ratio  $r_Q$  vs coupling gap  $g$ . Dashed (solid) lines refer to the dispersive (nondispersive) case.  $r_Q$  is the same in both cases and critical coupling is achieved for  $g = 2.2 \mu\text{m}$ .

expressions for the stored energy [Eqs. (A5)] are used in the numerator of Eq. (9).

Note that both  $\kappa_s^{\text{Kerr}} \propto 1/W_{\text{res}}^2$  [Eq. (A4c)] and  $Q_i \propto W_{\text{res}}$  [Eq. (9)] are affected when dispersion is ignored due to the erroneous zeroing of the  $W_j$  term [Eq. (A5c)]. However, the characteristic power [Fig. 3(c)] remains unaffected since it is proportional to the  $\kappa_s^{\text{Kerr}} Q_i^2$  product [Eqs. (6) and (A3)]. We find a minimum (due to the different trends between  $\kappa_s^{\text{Kerr}}$  and  $Q_i$ ) of  $P_0 = 75.6 \mu\text{W}$  for  $R = 10.1 \mu\text{m}$ . The respective mode has an azimuthal order  $m = 15$  with  $Q_i^{\text{disp}} = 2080$  and  $\kappa_s^{\text{Kerr,disp}} = 1.654$ .

Having determined the optimum radius, we side-couple the resonator with an access waveguide and seek to satisfy the  $r_Q = 1$  condition to specify the required gap for critical coupling [no TPA is present, i.e.  $r_{\text{TPA}} = 0$  in Eq. (8)]. To find it, we simulate the coupled ring-waveguide system and calculate the loaded quality factor  $Q$ , which is connected to the external quality factor  $Q_e$  through  $Q_e^{-1} = Q^{-1} - Q_i^{-1}$ . The  $Q$ -factor definition [Eq. (9)] is also used here to ensure that dispersion is correctly taken into account. The results are shown in Fig. 4. As was the case with  $Q_i$ , the external quality factor  $Q_e$  differs between the dispersive and nondispersive case. However, their ratio  $r_Q$  remains unaffected, since the dependence on stored energy cancels out. Critical coupling is achieved for a gap of  $g = 2.2 \mu\text{m}$  at a resonance frequency of  $f_0^{\text{disp}} = 10.014 \text{ THz}$ .

Having specified the radius and the coupling gap for the physical system, we can turn to Eqs. (5) and calculate its bistable response. Since no TPA is present, we set  $r_{\text{TPA}} = 0$  and use a normalized detuning  $\delta^{\text{disp}} = -1.5\delta_{\text{th}}$  ( $\Delta f = -12.5 \text{ GHz}$ ) to obtain optical bistability, as a compromise between the span of the bistability loop and the power at which it appears. This condition corresponds to  $\delta^{\text{non}} = -0.75\delta_{\text{th}}$ , indicating that no bistability is expected when dispersion is erroneously neglected. This

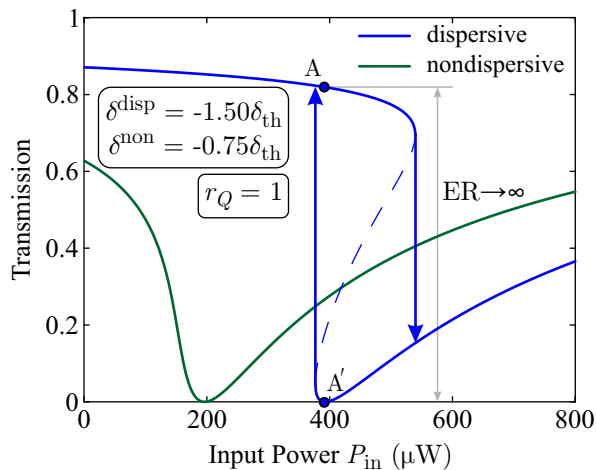


FIG. 5. Transmission vs input power for dispersive (blue) and nondispersive (green) cases. Infinite-ER bistable response is achieved at  $P_{\text{in}} = 400 \mu\text{W}$  for the dispersive case. For the same operating frequency, no bistability is obtained when dispersion is neglected: a consequence of the 2-fold difference between the respective  $Q$ -factors.

is verified by the results depicted in Fig. 5. Bistability is obtained only for the dispersive case with theoretically infinite ER, since the critical coupling condition has been satisfied. Bistable states A and A' are accessed with only  $400 \mu\text{W}$  of input power, demonstrating the potential of the proposed structure for practical applications. Importantly, the response time is only limited by the cavity lifetime  $\tau_i = 66 \text{ ps}$ , corresponding to bit rates in the order of 10 Gbps.

#### IV. NEAR-INFRARED REGIME

We now turn to the near-infrared frequency regime which is important for telecommunication applications. As in Sec. III, we focus on a side-coupled traveling-wave resonator for observing bistability. The system is based on the silicon-on-insulator technology and graphene is incorporated for contributing its nonlinearity. Since silicon is also nonlinear, we distinguish between the respective contributions to the overall nonlinearity, highlighting the capability of the proposed framework to handle multiple nonlinear materials of both bulk and sheet nature.

##### A. Graphene-Comprising Si-Slot Waveguide

In the NIR regime, graphene does not support SPPs and thus cannot be used as the main waveguiding mechanism. This is mainly because of the interband absorption process, allowed due to the high energy of the NIR photons. Thus, the total electrical conductivity of graphene is the sum of the intraband and the interband terms. In our design where low loss is important, we choose

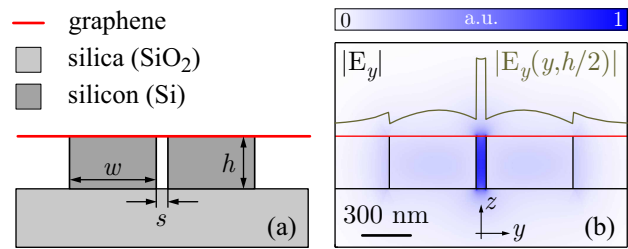


FIG. 6. (a) Si-slot waveguide with a graphene sheet on top. (b) Supported mode profile.  $E_y$ , the dominant component is tangential to the graphene sheet, maximizing the interaction.

an experimentally achievable Fermi level of  $0.45 \text{ eV}^{36}$  to suppress interband absorption (photon energy is  $0.8 \text{ eV}$  at  $1.55 \mu\text{m}$ ), resulting in a conductivity  $\sigma_1$  (Table III, Appendix B). That is because interband absorption is strong (resulting in high loss) only when the Fermi level of graphene is kept below half of the photon energy,  $\hbar\omega/2$ . For higher Fermi level values (as in our configuration), interband absorption is restricted due to Pauli blocking.<sup>37</sup>

The nonlinear properties of graphene in the NIR have recently been measured using different and independent experimental methods.<sup>17–19</sup> All measurements indicate that it acts as a de-focusing material (in contrast with the FIR) with a very high equivalent nonlinear parameter  $n_2 \approx -10^{-13} \text{ m}^2/\text{W}$ . It also exhibits significant TPA-induced nonlinear loss with an equivalent coefficient  $\beta_{\text{TPA}} \approx 0.9 \times 10^{-7} \text{ m/W}$  (in the THz,  $\beta_{\text{TPA}} = 0$ ) and low linear loss saturation when  $\hbar\omega < 2\mu_c$ ,<sup>30</sup> as in the case considered here. To introduce the measured values in our formulation, we must transform them into a (complex) surface nonlinear conductivity term. We should be extra careful with the transformation process since the presence of linear loss may cause an interplay between Kerr and TPA coefficients. Using Ref. 38, we can calculate the bulk-equivalent  $\chi^{(3)}$  parameter of graphene, connected with its nonlinear conductivity through<sup>39</sup>

$$\sigma_3 = j\omega\varepsilon_0 d_{\text{gr}}\chi^{(3)}, \quad (10)$$

where  $d_{\text{gr}} = 0.34 \text{ nm}$  is the thickness of a single graphene layer. We finally get a complex  $\sigma_3$  (Table III, Appendix B), with the real part representing TPA and the imaginary part the Kerr effect. It is easy to validate that TPA is relatively intense and must be taken into account ( $|\sigma_{3,\text{Re}}|/|\sigma_{3,\text{Im}}| = 0.1096$ ).

Although graphene has a highly nonlinear response in the optical regime, it cannot itself confine light, as the positive imaginary part of its linear conductivity implies. Thus we seek for a platform that can provide strong light confinement and maximum interaction with graphene. We choose the silicon-slot platform for its simple fabrication, the overall low loss it exhibits and the high confinement of light in the slot region.<sup>40</sup> A waveguide schematic is depicted in Fig. 6(a) where two silicon wires with cross-section dimensions  $w \times h = 360 \times 180 \text{ nm}$  are placed side-by-side on the top of a silica substrate to form a slot

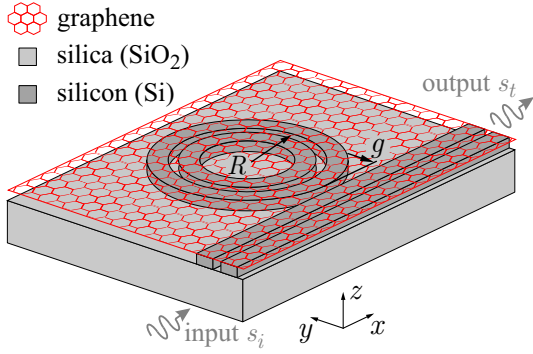


FIG. 7. Si-slot-based ring resonator, side-coupled to a bus waveguide of the same type. A graphene sheet is placed on top of the structure to contribute its nonlinearity.

TABLE II. Resonator radius  $R$  and resonance wavelength  $\lambda_0$  for various mode orders  $m$  of the graphene-comprising, Si-slot ring resonator.

$m$	$R$ ( $\mu\text{m}$ )	$\lambda_0^{\text{disp}}$ ( $\mu\text{m}$ )
17	2.08	1.5506
18	2.21	1.5507
19	2.34	1.5509
20	2.47	1.5512
21	2.60	1.5515
22	2.73	1.5518
23	2.86	1.5521
24	2.99	1.5525
25	3.12	1.5529
26	3.25	1.5533
27	3.38	1.5536
28	3.51	1.5540

with width  $s = 40$  nm. The 40-nm gap may sound challenging, but progress in modern fabrication techniques allows for gaps in straight slot waveguides as narrow as 10 nm.<sup>41</sup> A graphene sheet is placed on the top of the waveguide having maximum interaction with the dominant  $E_y$ -component of the supported mode [Fig. 6(b)]. Regarding Si and SiO<sub>2</sub> linear properties, we use the full Sellmeier formulas to take dispersion into account,<sup>42,43</sup> while we also consider Si nonlinear properties:  $n_{2,\text{Si}} = 2.5 \times 10^{-18}$  m<sup>2</sup>/W and  $\beta_{\text{TPA,Si}} = 5 \times 10^{-12}$  m/W. Note that  $n_{2,\text{Si}}$  is positive, in contrast with graphene respective parameter. Hence, the two nonlinearly-induced refractive index changes act in opposition, with the former increasing and the latter reducing the effective refractive index. Still, graphene nonlinearity is expected to dominate since (i) it is strong and (ii) the field penetration in Si is weak [line-plot in Fig. 6(b)].

## B. Ring-Waveguide System Design and Performance

The 3D graphene-comprising ring resonator, based on the Si-slot waveguide, is shown in Fig. 7. The geometrical

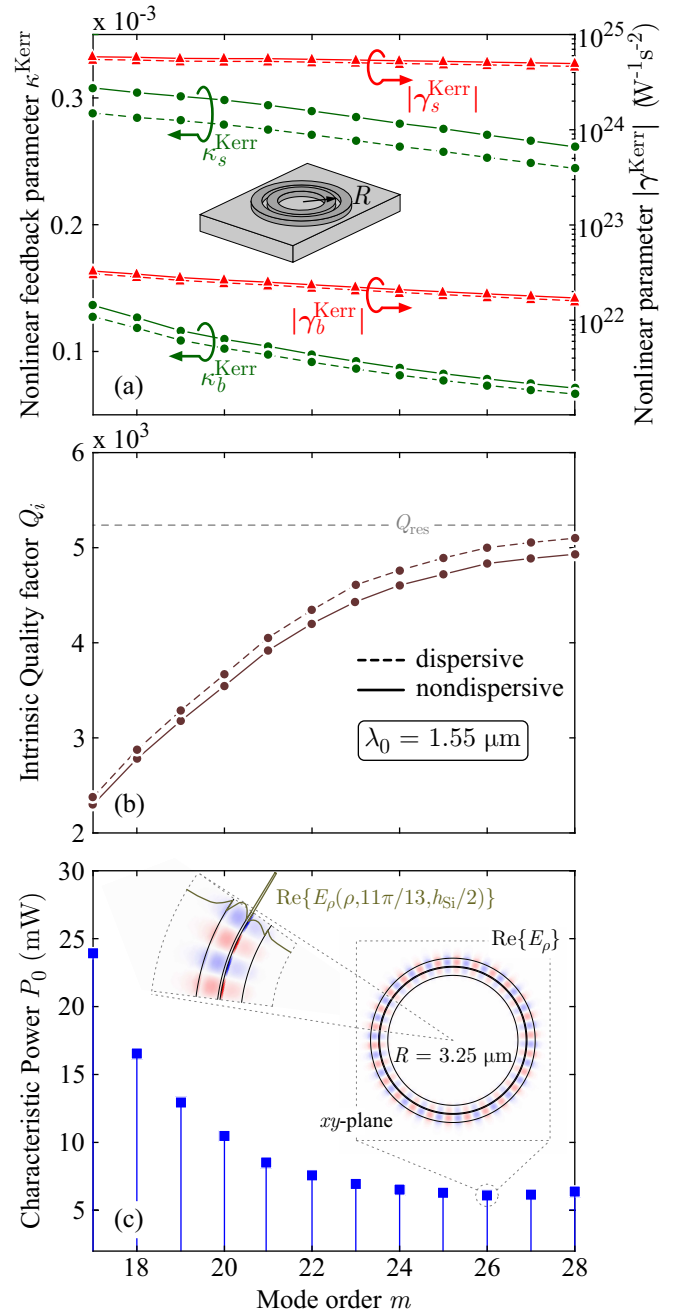


FIG. 8. (a) Nonlinear feedback parameters  $\kappa^{\text{Kerr}}$  and nonlinear parameters  $\gamma^{\text{Kerr}}$  vs mode order  $m$ . Graphene nonlinearity clearly dominates over Si. (b) Intrinsic quality factor  $Q_i$  vs  $m$ . (c) System characteristic power  $P_0$  vs  $m$ . Minimum  $P_0 = 6.1$  mW is obtained for  $m = 26$  ( $R = 3.25$   $\mu\text{m}$ ). Inset:  $\text{Re}\{E_\rho\}$  for the optimum mode. Dashed (solid) lines concern the dispersive (nondispersive) case. All quantities are discrete; the solid/dashed lines are used to guide the eye.

parameters, i.e. the radius  $R$  of the ring (measured at the center of the slot) and the coupling gap  $g$  is to be specified to obtain low-power optical bistability with high ER.

For the design process, we follow the steps presented in Sec. III A and record the azimuthal mode order  $m$  with

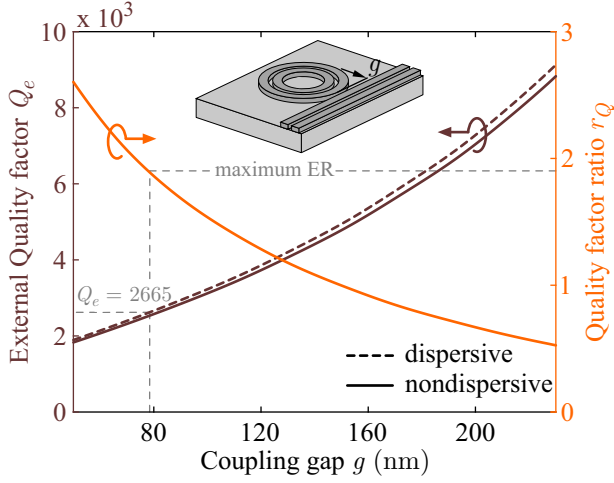


FIG. 9. External quality factor  $Q_e$  and quality factor ratio  $r_Q$  vs coupling gap  $g$ . Dashed (solid) lines refer to the dispersive (nondispersive) case. Maximum ER (zero transmission) is obtained for  $r_Q = 1.9$  ( $g = 78$  nm) instead of  $r_Q = 1$  ( $g = 150$  nm) due to TPA modifying the critical coupling condition.

the respective radius  $R$  and resonant wavelength  $\lambda_0$  in Table II. Subsequently, since both graphene and Si experience nonlinearities, we calculate separately the two respective nonlinear feedback parameters and plot them versus  $m$  in Fig. 8(a). It is clear that  $\kappa_s^{\text{Kerr}}$  is more than 3 times greater than  $\kappa_b^{\text{Kerr}}$ . Note that the effect of dispersion is less pronounced compared to the FIR example, since graphene dispersion is weak in the NIR. Nonetheless,  $\kappa$  parameters cannot be used for direct comparison of the strength of each nonlinear mechanism contribution. The appropriate parameters for comparison, which can be added directly, are the nonlinear parameters  $\gamma^{\text{Kerr}}$ , also plotted in Fig. 8(a). They differ by more than 2 orders of magnitude, reflecting that graphene nonlinearity is dominant. The intense electromagnetic field in the slot region is tangential and strongly interacts with the highly-nonlinear graphene sheet resulting in high values of  $\gamma_s^{\text{Kerr}}$ . On the other hand, the weaker Kerr coefficient of Si combined with the marginal field penetration in the material [inset of Fig. 8(c)] leads to poor values of  $\gamma_b^{\text{Kerr}}$  justifying this large difference.

The intrinsic quality factor is plotted in Fig. 8(b) as a function of the azimuthal order  $m$ . It increases with  $m$  until reaching the resistive loss ceiling, as expected. Optimum performance [Fig. 8(c)] is achieved for a radius of  $R = 3.25$   $\mu\text{m}$ , supporting a resonant mode with azimuthal order  $m = 26$ , resulting in an extremely low characteristic power of  $P_0 = 6.1$  mW, with  $Q_i = 5017$ ,  $\kappa_s^{\text{Kerr}} = 0.2529 \times 10^{-3}$  and  $\kappa_b^{\text{Kerr}} = 0.0732 \times 10^{-3}$ .

For the side-coupled system,  $r_Q = 1$  is met for a coupling gap of  $g = 150$  nm, as shown in Fig. 9, where we plot the external quality factor and the quality factor ratio versus  $g$ . This value is not expected to give zero transmission on resonance due to TPA; the respective strength factor (taking also Si-induced TPA into ac-

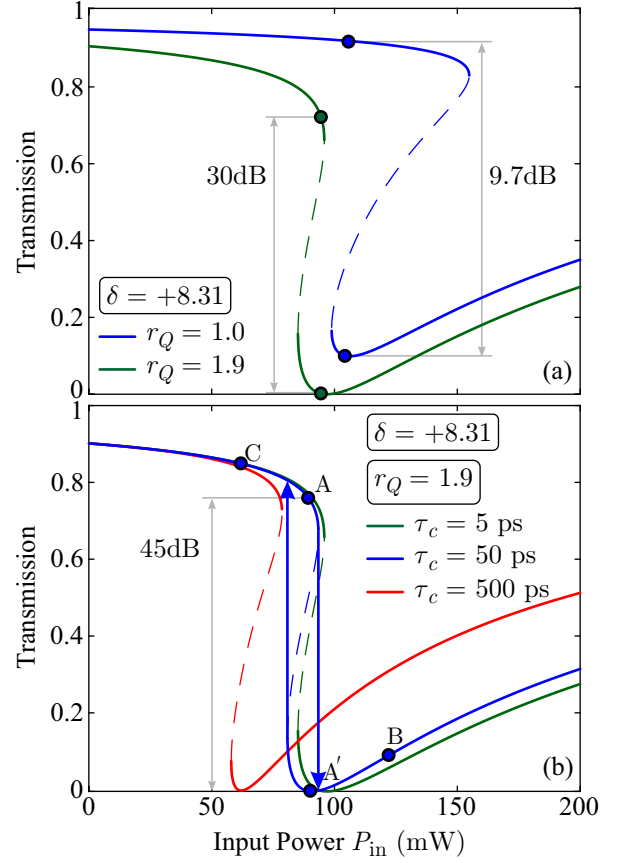


FIG. 10. (a) Bistability curves for different quality factor ratios without FCEs. Minimum transmission (maximum ER) is obtained for  $r_Q = 1.9$ . (b) Bistability curves for different carrier lifetimes. For  $\tau_c = 50$  ps, zero transmission is obtained, giving an ER of 45 dB at  $P_{\text{in}} = 91$  mW. For  $\tau_c = 5$  ps, the loop of subfigure (a) is recovered, indicating that FCEs are negligible. Only the dispersive case is considered.

count) is equal to  $r_{\text{TPA}} = 0.1109$ . Returning in Eq. (8), we find that zero transmission and thus maximum ER is obtained for  $r_Q = 1.9$  at a coupling gap of  $g = 78$  nm. This value is calculated for a specific normalized stored energy on resonance ( $|\tilde{u}|^2 = 8$ ) and it corresponds to a  $Q_e = 2665$  at the resonance wavelength  $\lambda_0 = 1.556$   $\mu\text{m}$ .

This is indeed verified by Fig. 10(a) where the nonlinear response of the resonant structure is obtained after solving Eqs. (5), using a positive detuning  $\delta = 8.31$  ( $\Delta\lambda = -1.3$  nm), since graphene nonlinearity blue-shifts the resonance frequency. In the proposed system, we must also take into account the effect of the free carriers, generated on silicon via the TPA process. Using the method presented in Ref. 15 we find that carrier-induced nonlinearities (free carrier effects, FCEs) are moderately weak, with the respective strength factors quantifying the contribution of free carrier dispersion (FCD) and free carrier absorption (FCA) relative to the Kerr effect being equal to  $7.3 \times 10^{-3}$  and  $0.24 \times 10^{-3}$ , respectively, assuming an input power of  $P_{\text{in}} = 90$  mW and a carrier lifetime of  $\tau_c = 50$  ps. This lifetime is achievable using

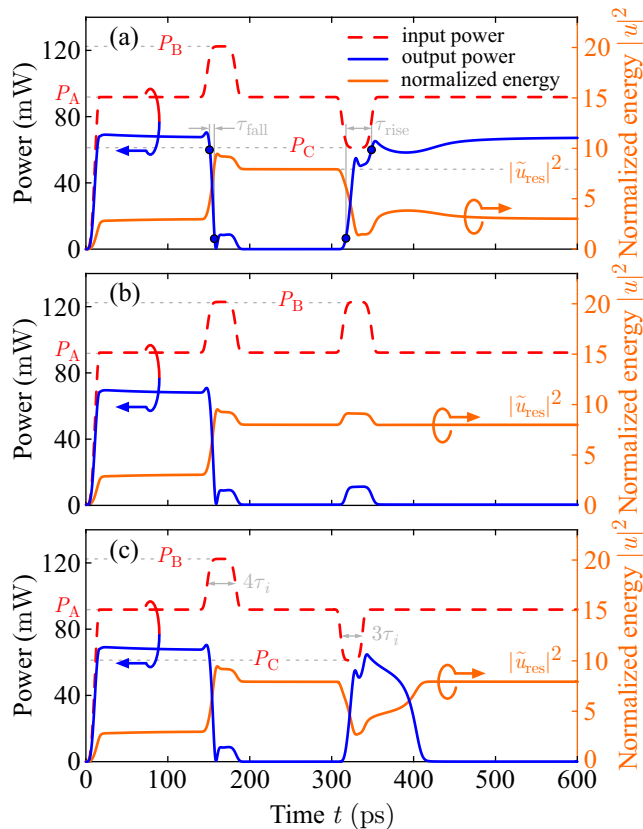


FIG. 11. Memory operation of the bistable device for  $\tau_c = 50$  ps and  $r_Q = 1.9$ . (a) Set and Reset pulses for toggling between bistable states by following route ABA'CA of the CW curve in Fig. 10(b). Super Gaussian pulses with a FWHM of  $4\tau_i$  are used. (b) A second Set pulse does not change the state of the system. (c) A Reset pulse of short duration (FWHM =  $3\tau_i$ ) does not succeed in toggling the system state due to the finite cavity photon lifetime.

ion implantations in Si without inducing significant linear loss in the supported mode.<sup>44,45</sup> It is important to note that FCD also blue-shifts the resonant frequency, as Kerr nonlinearity in graphene does, thus acting constructively. Nevertheless, FCD responds in time scales of the order of  $\tau_c$  (Kerr effect is instantaneous) justifying the need to reduce carrier lifetime from the typical value of 500 ps. Naturally, this action reduces the strength of FCD (and subsequently FCA), as Fig. 10(b) reveals, plotting the CW bistability loop for different carrier lifetimes. Larger  $\tau_c$  allows bistability to appear for lower input power, accompanied however with slower response times. Ultimately, bistable operating points A and A' are accessed with an input power of  $P_{in} = 90$  mW, having an almost infinite ER.

Various scenarios of the dynamic response of the proposed device acting as a memory module are investigated in Fig. 11. In the basic one, depicted in Fig. 11(a), we set the initial state at point A. Using a Set pulse reaching  $P_B = 122$  mW, a transition to the low power state A' is obtained, while a Reset pulse, dropping at  $P_C = 61$  mW,

returns the system to its initial state. Third-order super-Gaussian pulses are used, with a FWHM of  $4\tau_i = 33.2$  ps. The Set pulse causes fast switching (attributed to the small cavity lifetime,  $\tau_i = 8.3$  ps) with a fall time (90% – 10%) of 6.1 ps. The Reset process, on the other hand, is slower due to the extra carriers that are generated when the resonator is full and need to recombine.<sup>15</sup> Overall, the reset process has a rise time (10% – 90%) of 32 ps, allowing for switching rates of more than 20 GHz.

On other scenarios, we recognize in Fig. 11(b) that if, after a Set pulse, an extra Set pulse arrives, the device remains stable. This is also true if two consequent Reset pulses arrive. Additionally, we must note that due to the finite photon lifetime, the duration of the pulse cannot be too short, as Fig. 11(c) illustrates. In this case, the Reset pulse has a smaller FWHM ( $3\tau_i$ ) which cannot provide the conditions for the resonator to empty out and cause the switching action.

As a final remark, we note that Kerr-induced nonlinear frequency shift can be canceled out, taking advantage of the different sign between silicon and graphene nonlinearities. This is important for example in wavelength-division multiplexing (WDM) ring resonator filters where crosstalk between channels due to nonlinearity is considerable. More specifically, by moving the graphene sheet upwards, we can reduce its interaction with the mode, thus reducing  $\gamma_s^{Kerr}$  (in absolute value). On the other hand,  $\gamma_b^{Kerr}$  is constant, since the supported mode is not significantly affected. In the proposed structure, moving the graphene sheet at  $h = 115.6$  nm above Si results in a  $\gamma_s^{Kerr} = -1.77 \times 10^{22} \text{ W}^{-1}\text{s}^{-2}$ , exactly canceling the Kerr nonlinearity of silicon ( $\gamma_b^{Kerr} = 1.77 \times 10^{22} \text{ W}^{-1}\text{s}^{-2}$ ); in that case the resonator is linear since FCEs are weak due to the ion implants.

## V. CONCLUSION

To recapitulate, we have proposed practical, three-dimensional nonlinear resonant circuits for low-power Kerr-induced bistability by incorporating graphene into the structures and exploiting its unique nonlinear properties. Two systems have been carefully designed for operation in the FIR and NIR frequency regime, respectively. In the first case (THz regime), graphene is used for both guiding the wave (in the form of graphene plasmon polaritons) as well as contributing its nonlinearity. High-quality bistable response with high extinction ratio between bistable states is achieved with an ultra-low input power of only 400  $\mu\text{W}$ . In the second case (NIR), waveguiding is performed with a silicon photonic platform and a graphene sheet is placed on top for contributing its nonlinearity. The silicon-slot geometry is judiciously chosen so as to maximize the interaction between graphene and the guided wave. As a result, bistability is obtained with an input power of only 90 mW; a remarkable performance for Kerr-induced bistability in the NIR regime given that TPA and FCEs are taken into account, with their influ-

ence carefully minimized during the design process. Importantly, having utilized the instantaneous Kerr effect, the proposed components allow for fast dynamic operation. Their response time is only limited by the photon cavity and free carrier lifetime.

For analyzing the structures we have made use of a recently-developed mathematical framework combining perturbation theory and coupled-mode theory. The framework allows for accurate and efficient modeling of nonlinear resonators comprising both bulk and sheet materials. Importantly, we have shown that the strong linear dispersion of graphene must be taken into account, since it significantly impacts the nonlinear response.

In conclusion, the proposed components highlight the potential of graphene as a nonlinear material over a vast frequency range, from few THz to the NIR regime. Besides the memory operation demonstrated, the designed systems can be also utilized for cross-phase modulation and/or four-wave mixing, extending the range of practical applications.

## ACKNOWLEDGMENTS

The authors would like to express their gratitude to Mr. Georgios Sinatkas for his useful comments throughout the preparation of the manuscript.

## Appendix A: Notes on the Formulation

To obtain Eq. (2) from Eq. (1) we express the nonlinear polarization and the nonlinear current density in terms of the applied electric field, allowing  $\chi^{(3)}$  susceptibility and  $\sigma_3$  conductivity to be complex, in order to model both Kerr effect and TPA. In this case, the isotropic bulk nonlinear polarization can be written as

$$\mathbf{P}_{\text{NL}} = \frac{1}{4} \varepsilon_0 \chi^{(3)} [2(\mathbf{E}_0 \cdot \mathbf{E}_0^*) \mathbf{E}_0 + (\mathbf{E}_0 \cdot \mathbf{E}_0) \mathbf{E}_0^*], \quad (\text{A1})$$

while for sheet-type materials described by a surface conductivity term (such as graphene), we write the nonlinear current density as<sup>39</sup>

$$\mathbf{J}_{\text{NL}} = \frac{\sigma_3}{4} \left[ 2(\mathbf{E}_{0,\parallel} \cdot \mathbf{E}_{0,\parallel}^*) \mathbf{E}_{0,\parallel} + (\mathbf{E}_{0,\parallel} \cdot \mathbf{E}_{0,\parallel}) \mathbf{E}_{0,\parallel}^* \right] \delta_s(\mathbf{r}), \quad (\text{A2})$$

with the symbol  $\mathbf{E}_{0,\parallel}$  denoting the tangential to the sheet electric field components (out-of-plane component does not interact with the sheet material), and  $\delta_s(\mathbf{r})$  is the surface Dirac function. Nonlinear terms of Eqs. (A1) and (A2) describe a specific, yet very practical situation. In a more general case (e.g. anisotropic nonlinearities), any valid expression for polarization and/or current density can be used to calculate the complex  $\Delta\omega$  using Eq. (1).

Substituting Eqs.(A1) and (A2) in Eq. (1) we find the nonlinear parameters  $\gamma$  equal to

$$\gamma_b^{\text{Kerr}} = 4 \left( \frac{\omega_0}{c_0} \right)^3 \omega_0 c_0 \kappa_b^{\text{Kerr}} n_2^{\text{max}}, \quad (\text{A3a})$$

$$\gamma_b^{\text{TPA}} = 2 \left( \frac{\omega_0}{c_0} \right)^3 c_0^2 \kappa_b^{\text{TPA}} \beta_{\text{TPA}}^{\text{max}}, \quad (\text{A3b})$$

$$\gamma_s^{\text{Kerr}} = \left( \frac{\omega_0}{c_0} \right)^4 \kappa_s^{\text{Kerr}} \frac{\sigma_{3,\text{Im}}^{\text{max}}}{\varepsilon_0^2}, \quad (\text{A3c})$$

$$\gamma_s^{\text{TPA}} = \left( \frac{\omega_0}{c_0} \right)^4 \kappa_s^{\text{TPA}} \frac{\sigma_{3,\text{Re}}^{\text{max}}}{\varepsilon_0^2}, \quad (\text{A3d})$$

different for each nonlinear phenomenon (Kerr effect, TPA) and material type (bulk, sheet). The dimensionless nonlinear feedback parameters  $\kappa$  appearing in Eqs. (A3) are defined as

$$\kappa_b^{\text{Kerr}} = \left( \frac{c_0}{\omega_0} \right)^3 \frac{\frac{1}{3} \int_V n_2 n^2 (2|\mathbf{E}_0|^4 + |\mathbf{E}_0 \cdot \mathbf{E}_0|^2) dV}{\left[ \int_V \frac{\partial\{\omega\varepsilon_r\}}{\partial\omega} |\mathbf{E}_0|^2 dV + \eta_0^2 \int_V |\mathbf{H}_0|^2 dV + \frac{1}{\varepsilon_0} \int_S \frac{\partial\sigma_{1,\text{Im}}}{\partial\omega} |\mathbf{E}_{0,\parallel}|^2 dS \right]^2} n_2^{\text{max}}, \quad (\text{A4a})$$

$$\kappa_b^{\text{TPA}} = \left( \frac{c_0}{\omega_0} \right)^3 \frac{\frac{1}{3} \int_V \beta_{\text{TPA}} n^2 (2|\mathbf{E}_0|^4 + |\mathbf{E}_0 \cdot \mathbf{E}_0|^2) dV}{\left[ \int_V \frac{\partial\{\omega\varepsilon_r\}}{\partial\omega} |\mathbf{E}_0|^2 dV + \eta_0^2 \int_V |\mathbf{H}_0|^2 dV + \frac{1}{\varepsilon_0} \int_S \frac{\partial\sigma_{1,\text{Im}}}{\partial\omega} |\mathbf{E}_{0,\parallel}|^2 dS \right]^2} \beta_{\text{TPA}}^{\text{max}}, \quad (\text{A4b})$$

$$\kappa_s^{\text{Kerr}} = \left( \frac{c_0}{\omega_0} \right)^4 \frac{\int_S \sigma_{3,\text{Im}} (2|\mathbf{E}_{0,\parallel}|^4 + |\mathbf{E}_{0,\parallel} \cdot \mathbf{E}_{0,\parallel}|^2) dS}{\left[ \int_V \frac{\partial\{\omega\varepsilon_r\}}{\partial\omega} |\mathbf{E}_0|^2 dV + \eta_0^2 \int_V |\mathbf{H}_0|^2 dV + \frac{1}{\varepsilon_0} \int_S \frac{\partial\sigma_{1,\text{Im}}}{\partial\omega} |\mathbf{E}_{0,\parallel}|^2 dS \right]^2} \sigma_{3,\text{Im}}^{\text{max}}, \quad (\text{A4c})$$

$$\kappa_s^{\text{TPA}} = \left(\frac{c_0}{\omega_0}\right)^4 \frac{\int_S \sigma_{3,\text{Re}} (2|\mathbf{E}_{\mathbf{0},\parallel}|^4 + |\mathbf{E}_{\mathbf{0},\parallel} \cdot \mathbf{E}_{\mathbf{0},\parallel}|^2) dS}{\left[ \int_V \frac{\partial\{\omega\varepsilon_r\}}{\partial\omega} |\mathbf{E}_{\mathbf{0}}|^2 dV + \eta_0^2 \int_V |\mathbf{H}_{\mathbf{0}}|^2 dV + \frac{1}{\varepsilon_0} \int_S \frac{\partial\sigma_{1,\text{Im}}}{\partial\omega} |\mathbf{E}_{\mathbf{0},\parallel}|^2 dS \right]^2} \sigma_{3,\text{Re}}^{\text{max}}. \quad (\text{A4d})$$

They all measure the mode overlap with each nonlinear material and they are independent of the input power, the quality factor and the coupling conditions, characterizing the system overall.<sup>10</sup> Note that when an eigenvalue simulation is used to estimate  $\kappa$  in traveling-wave resonators, the obtained result should be corrected with a factor of approximately 2/3. This is physically and mathematically strict for 2D problems,<sup>25</sup> but our weakly-coupled harmonic propagation simulations (which is always the correct approach to estimate  $\kappa$ ) reveals that this correction coefficient approximately holds for the 3D geometries examined in this work as well.

Also note that the denominators of  $\kappa$  are all proportional to the stored energy in the resonator. The three respective terms, corresponding to dispersive electric, magnetic and current density energy are given by<sup>25</sup>

$$W_e = \frac{1}{4} \int_V \frac{\partial\{\omega\varepsilon_0\varepsilon_r(\omega)\}}{\partial\omega} \Big|_{\omega=\omega_0} |\mathbf{E}_{\mathbf{0}}|^2 dV, \quad (\text{A5a})$$

$$W_m = \frac{1}{4} \int_V \mu_0 |\mathbf{H}_{\mathbf{0}}|^2 dV, \quad (\text{A5b})$$

$$W_j = \frac{1}{4} \int_S \frac{\partial\sigma_{1,\text{Im}}(\omega)}{\partial\omega} \Big|_{\omega=\omega_0} |\mathbf{E}_{\mathbf{0},\parallel}|^2 dS, \quad (\text{A5c})$$

while the total stored energy is the sum of the three terms,  $W_{\text{res}} = W_e + W_m + W_j$ . Finally, it is worth noting that, when  $\sigma_{1,\text{Im}} \neq 0$ , the equality between electric and magnetic energy on resonance is lifted.

## Appendix B: Graphene Properties

Regarding its linear properties, graphene conductivity originates from two absorption mechanisms, namely the intraband and the interband absorption. That is because of its unique energy diagram, which is conoidal-shaped near the Dirac point, having a zero band-gap. The intraband absorption mechanism exhibit a Drude-like behaviour like common metals, modeled by<sup>46,47</sup>

$$\sigma_{\text{intra}} = -j \frac{e^2 \mu_c}{\pi \hbar^2 (\omega - j/\tau_1)} \frac{2k_B T}{\mu_c} \ln \left[ 2 \cosh \left( \frac{\mu_c}{2k_B T} \right) \right], \quad (\text{B1})$$

where  $e$  is the electron charge,  $\hbar$  is the reduced Planck constant,  $k_B$  is the Boltzmann constant,  $T = 300$  K is the absolute temperature,  $\mu_c$  is the Fermi level and  $\tau_1$  is the relaxation time for intraband absorption, phenomenologically measuring the purity of graphene. In the FIR we set  $\tau_1 = 40$  ps, while in the NIR  $\tau_1 = 10$  fs.

TABLE III. Graphene conductivity (linear and nonlinear), used for the dispersionless simulations in the FIR and NIR.

	FIR (10 THz)	NIR (1.55 $\mu\text{m}$ )
$\sigma_1$ [ $\mu\text{S}$ ]	$0.52 - j1311$	$3.67 + j11.58$
$\sigma'_1$ [ $\mu\text{S}$ ]	$0.26 - j560$	-
$\sigma_3$ [ $\text{S}(\text{m}/\text{V})^2$ ]	$j0.633 \times 10^{-19}$	$(0.607 - j5.54) \times 10^{-21}$
$\sigma'_3$ [ $\text{S}(\text{m}/\text{V})^2$ ]	$j1.48 \times 10^{-19}$	-

Interband absorption, on the other hand, is modeled by<sup>46</sup>

$$\sigma_{\text{inter}} = -j \frac{e^2}{4\pi\hbar} \ln \left[ \frac{2|\mu_c| - \hbar(\omega - j/\tau_2)}{2|\mu_c| + \hbar(\omega - j/\tau_2)} \right], \quad (\text{B2})$$

where  $\tau_2 = 1.2$  ps is the relaxation time for interband absorption. The two different contributions add-up to give the total linear conductivity of graphene.

Regarding graphene nonlinear properties, in the FIR where interband transitions are not allowed, there is a closed-form expression for the nonlinear conductivity which reads<sup>20</sup>

$$\sigma_3 = j \frac{3e^4 v_F^2}{32\pi\omega^3 \hbar^2 \mu_c}, \quad (\text{B3})$$

where  $v_F \approx c_0/300$  is the Fermi velocity in graphene. In the NIR, however, there is not a similarly simple expression<sup>31</sup> and we thus rely on the measured values presented in Sec. IV A. In Table III we gather all the values of  $\sigma_1$  and  $\sigma_3$  that are used in the main text for the dispersionless case; in the dispersive case Eqs. (B1) and (B2) are used.

- <sup>1</sup>J. Leuthold, C. Koos, and W. Freude, *Nat. Photon.* **4**, 535 (2010).
- <sup>2</sup>M. Kauranen and A. V. Zayats, *Nat. Photon.* **6**, 737 (2012).
- <sup>3</sup>T. Tanabe, M. Notomi, S. Mitsugi, A. Shinya, and E. Kuramochi, *Opt. Lett.* **30**, 2575 (2005).
- <sup>4</sup>M. Notomi, A. Shinya, S. Mitsugi, G. Kira, E. Kuramochi, and T. Tanabe, *Opt. Expr.* **13**, 2678 (2005).
- <sup>5</sup>M. F. Yanik, S. Fan, and M. Soljačić, *Appl. Phys. Lett.* **83**, 2739 (2003).
- <sup>6</sup>Q. Xu and M. Lipson, *Opt. Expr.* **15**, 924 (2007).
- <sup>7</sup>B. A. Daniel and G. P. Agrawal, *J. Opt. Soc. Am. B* **27**, 956 (2010).
- <sup>8</sup>B. Maes, P. Bienstman, and R. Baets, *J. Opt. Soc. Am. B* **22**, 1778 (2005).
- <sup>9</sup>D. A. Ketzaki, O. Tsilipakos, T. V. Yioultsis, and E. E. Kriezis, *J. Appl. Phys.* **114**, 113107 (2013).
- <sup>10</sup>M. Soljačić, M. Ibanescu, S. G. Johnson, Y. Fink, and J. D. Joannopoulos, *Phys. Rev. E* **66**, 055601 (2002).
- <sup>11</sup>A. Pannipitiya, I. D. Rukhlenko, and M. Premaratne, *J. Opt. Soc. Am. B* **28**, 2820 (2011).

- <sup>12</sup>X. Wang, H. Jiang, J. Chen, P. Wang, Y. Lu, and H. Ming, *Opt. Expr.* **19**, 19415 (2011).
- <sup>13</sup>T. Christopoulos, G. Sinatkas, O. Tsilipakos, and E. E. Kriezis, *Opt. Quantum Electron.* **48**, 128 (2016).
- <sup>14</sup>O. Tsilipakos and E. E. Kriezis, *J. Opt. Soc. Am. B* **31**, 1698 (2014).
- <sup>15</sup>O. Tsilipakos, T. Christopoulos, and E. E. Kriezis, *J. Lightw. Technol.* **34**, 1333 (2016).
- <sup>16</sup>Q. Bao and K. P. Loh, *ACS Nano* **6**, 3677 (2012).
- <sup>17</sup>E. Dremetsika, B. Dlubak, S.-P. Gorza, C. Ciret, M.-B. Martin, S. Hofmann, P. Seneor, D. Dolfi, S. Massar, P. Emplit, and P. Kockaert, *Opt. Lett.* **41**, 3281 (2016).
- <sup>18</sup>N. Vermeulen, D. Castelló-Lurbe, J. Cheng, I. Pasternak, A. Krajeska, T. Ciuk, W. Strupinski, H. Thienpont, and J. Van Erps, *Phys. Rev. Appl.* **6**, 044006 (2016).
- <sup>19</sup>G. Demetriou, H. T. Bookey, F. Biancalana, E. Abraham, Y. Wang, W. Ji, and A. K. Kar, *Opt. Expr.* **24**, 13033 (2016).
- <sup>20</sup>S. A. Mikhailov and K. Ziegler, *J. Phys.: Condens. Matter* **20**, 384204 (2008).
- <sup>21</sup>L. Zhang, J. Yang, X. Fu, and M. Zhang, *Appl. Phys. Lett.* **103**, 163114 (2013).
- <sup>22</sup>T. Gu, N. Petrone, J. F. McMillan, A. Van Der Zande, M. Yu, G. Q. Lo, D. L. Kwong, J. Hone, and C. W. Wong, *Nat. Photon.* **6**, 554 (2012).
- <sup>23</sup>C. Horvath, D. Bachman, R. Indoe, and V. Van, *Opt. Lett.* **38**, 5036 (2013).
- <sup>24</sup>T. Gu, J. F. McMillan, N. W. Petrone, A. Van Der Zande, J. C. Hone, M. Yu, G. Q. Lo, D. L. Kwong, and C. Wei Wong, *Opt. Commun.* **314**, 23 (2014).
- <sup>25</sup>T. Christopoulos, O. Tsilipakos, N. Grivas, and E. E. Kriezis, *Phys. Rev. E* **94**, 062219 (2016).
- <sup>26</sup>J. Bravo-Abad, S. Fan, S. Johnson, J. D. Joannopoulos, and M. Soljačić, *J. Lightw. Technol.* **25**, 2539 (2007).
- <sup>27</sup>H. A. Haus, *Waves and Fields in Optoelectronics* (Prentice-Hall, New Jersey, 1984).
- <sup>28</sup>S. V. Afshar and T. M. Monro, *Opt. Expr.* **17**, 2298 (2009).
- <sup>29</sup>P. N. Butcher and D. Cotter, *The elements of nonlinear optics* (Cambridge University Press, Cambridge, 1990).
- <sup>30</sup>A. Marini, J. D. Cox, and F. J. García de Abajo, *Phys. Rev. B* **95**, 125408 (2017).
- <sup>31</sup>J. L. Cheng, N. Vermeulen, and J. E. Sipe, *New J. Phys.* **16**, 053014 (2014).
- <sup>32</sup>X. Wu and X. Guo, *Sci. Rep.* **7** (2017).
- <sup>33</sup>J. Zheng, L. Yu, S. He, and D. Dai, *Sci. Rep.* **5** (2015).
- <sup>34</sup>H. J. Xu, W. B. Lu, Y. Jiang, and Z. Gao Dong, *Appl. Phys. Lett.* **100**, 051903 (2012).
- <sup>35</sup>A. Raman and S. Fan, *Phys. Rev. B* **83**, 205131 (2011).
- <sup>36</sup>V. Soriano, G. De Angelis, T. Cassese, M. Midrio, M. Romagnoli, M. Mohsin, M. Otto, D. Neumaier, I. Asselberghs, J. Van Campenhout, and C. Huyghebaert, *Opt. Expr.* **24**, 29984 (2016).
- <sup>37</sup>Z. Q. Li, E. A. Henriksen, Z. Jiang, Z. Hao, M. C. Martin, P. Kim, H. L. Stormer, and D. N. Basov, *Nat. Phys.* **4**, 832 (2008).
- <sup>38</sup>R. del Coso and J. Solis, *J. Opt. Soc. Am. B* **21**, 640 (2004).
- <sup>39</sup>D. Chatzidimitriou, A. Ptilakis, and E. E. Kriezis, *J. Appl. Phys.* **118**, 023105 (2015).
- <sup>40</sup>W. Zhang, S. Serna, X. Le Roux, C. Alonso-Ramos, L. Vivien, and E. Cassan, *Opt. Lett.* **40**, 5566 (2015).
- <sup>41</sup>K. Debnath, A. Z. Khokhar, G. T. Reed, and S. Saito, *IEEE Photonic. Tech. L.* **29**, 1269 (2017).
- <sup>42</sup>C. D. Salzberg and J. J. Villa, *J. Opt. Soc. Am.* **47**, 244 (1957).
- <sup>43</sup>I. H. Malitson, *J. Opt. Soc. Am.* **55**, 1205 (1965).
- <sup>44</sup>M. Först, J. Niehusmann, T. Plötzing, J. Bolten, T. Wahlbrink, C. Moormann, and H. Kurz, *Opt. Lett.* **32**, 2046 (2007).
- <sup>45</sup>M. Waldow, T. Plötzing, M. Gottheil, M. Först, J. Bolten, T. Wahlbrink, and H. Kurz, *Opt. Expr.* **16**, 7693 (2008).
- <sup>46</sup>G. W. Hanson, *J. Appl. Phys.* **103**, 064302 (2008).
- <sup>47</sup>L. A. Falkovsky, *Phys. Usp.* **51**, 887 (2008).